Geodesy and Geodynamics 17 (2026) 688–700

Contents lists available at ScienceDirect

Geodesy and Geodynamics

journal homepage: http://www.keaipublishing.com/geog

Research Paper

Estimating the velocities of space-geodetic stations: the case of DORIS

Sofiane Khelifa *, Saddam Housseyn Allal, Hicham Dekkiche

Centre of Space Techniques, Algerian Space Agency, Arzew 31200, Algeria

ARTICLE INFO

Article history:
Received 2 June 2025
Received in revised form
22 December 2025
Accepted 23 December 2025
Available online 11 March 2026

Keywords:
Geodetic station velocities
DORIS
Time series analysis
Global plate models

ABSTRACT

Velocity estimates derived from time series of space geodetic station positions are influenced by seasonal signals and noise present in these time series. Therefore, the insufficiently modeled trend of these time series will distort station velocity estimates and their uncertainties. In this study, velocities are estimated using two distinct approaches: Singular Spectrum Analysis (SSA) and Wavelet Multiresolution Analysis (WMA), both of which enable the reliable separation of trend from periodic signals and noise. The data used are the combined residual coordinate time series of 45 DORIS (Doppler Orbitography and Radiopositioning Integrated by Satellite) stations, aligned to ITRF2014 and expressed in a topocentric coordinate system (North, East, and Up). The SSA results reveal a dominant trend (velocity) in the horizontal components (North and East), with a variance exceeding 99% of the total signal for most stations. The estimates of horizontal velocities by SSA and WMA are almost similar and agree with those calculated from plate tectonic models (GSRM 2.1, ITRF2020, GEODVEL 2010, REVEL 2000, MORVEL 2010, and NUVEL 1A), except six stations: AMSTERDAM, DIONYSOS, EVEREST, MANAGUA, MANGILAO, and MANILLE. These stations, most of which are located at tectonic plate boundaries, have suffered great earthquakes with a magnitude above 6.0. The vertical velocities of DORIS and GPS (Global Positioning System) at 26 co-located sites vary from −3 mm/yr to 2 mm/yr, except for the high-latitude stations THULE (76.54°) and NY-ALESUND (78.92°), which exhibit high velocities of around 7.3 mm/yr and 6.7 mm/yr for DORIS, and 7.2 mm/yr and 8 mm/yr for GPS, respectively.

© 2026 Editorial office of Geodesy and Geodynamics. Publishing services by Elsevier B.V. on behalf of KeAi Communications Co. Ltd. This is an open access article under the CC BY-NC-ND license (http://creativecommons.org/licenses/by-nc-nd/4.0/).

1. Introduction

DORIS (Doppler Orbitography and Radiopositioning Integrated by Satellite) [1] is one of the space geodetic techniques, alongside GNSS (Global Navigation Satellite System) [2], SLR (Satellite Laser Ranging) [3], and VLBI (Very Long Baseline Interferometry) [4]. It is a French satellite tracking system designed by the CNES (Centre National d'Etudes Spatiales) in close cooperation with the IGN (Institut national de l'information Géographique et forestière) and the GRGS (Groupe de Recherche de Géodésie Spatiale). The French remote sensing satellite SPOT-2, launched on January 22, 1990, was the first scientific satellite carrying a DORIS receiver on board, while the SWOT altimeter satellite is the latest mission, launched on December 16, 2022. Beyond precise orbit determination (POD) of satellites, tracking the polar motion of the Earth, and detecting the current state of the ionosphere. DORIS is also sed for determining the positioning of ground stations and their velocities. A precise position measurement is made of the Doppler shift on radiofrequency signals emitted by ground stations and received on-board different satellites, carrying DORIS receivers. These measurements are processed by six Analysis Centers (ESA, GOP, GRG, GSC, IGN, and INA), providing solutions in the form of coordinate time series at weekly intervals. Every three months, the Analysis Centers submit these solutions to the International DORIS Service (IDS) [5], which includes weekly station positions, daily Earth Orientation Parameters (EOPs) and the full covariance matrix. After evaluation by the IDS combination Center, these solutions are combined in a standard least-squares adjustment to form the IDS weekly combined solutions.

Station coordinate time series derived from space techniques always exhibit seasonal signatures [6–9], mainly annual and semi-annual signals, with amplitudes of a few millimeters. Although the

* Corresponding author.
E-mail address: skhelifa@cts.asal.dz (S. Khelifa).

Peer review under the responsibility of Editorial office of Geodesy and Geodynamics.

https://doi.org/10.1016/j.geog.2025.12.009

1674-9847/© 2026 Editorial office of Geodesy and Geodynamics. Publishing services by Elsevier B.V. on behalf of KeAi Communications Co. Ltd. This is an open access article under the CC BY-NC-ND license (http://creativecommons.org/licenses/by-nc-nd/4.0/).

causes of annual and semi-annual signals are still not completely understood, the most plausible explanation is a combination of atmospheric and hydrological loadings [10–12]. The amplitudes of seasonal signals in the DORIS data have already been quantified by numerous authors [8,13–15] using various methodologies. Beyond seasonal signatures, several studies have been conducted to estimate the noise in space-geodetic positioning [14,16,17], primarily employing two statistical methods: maximum likelihood estimation [18] and Allan variance [19].

The velocities of space geodetic stations represent the linear displacement of the Earth's crust resulting from tectonic plate movements. Their estimation is significantly influenced by seasonal signals and noise contained in the station coordinates. The impact of seasonal signals and noise on the estimation of tectonic motion has been investigated through various approaches to modeling seasonal signals and noise in station coordinate time series [15,20–23]. This study aims to reliably estimate DORIS stations' velocities by extracting the trend separately from seasonal signals and noise, using two different methods: Singular Spectrum Analysis (SSA) and Wavelet Multiresolution Analysis (WMA). The SSA [24], based on the phase space, allows for the decomposition of a time series into its three distinct components, such as trend, oscillatory components, and noise. The WMA [25] enables the study of a time series over various scales (or resolutions) by employing functions (wavelets) that are well-localized in the both time and frequency domains, derived from one another through translation and dilation.

This paper is organized as follows. In Section 2, we provide a brief overview of the mathematical formalisms of the tools employed in our study, namely SSA and WMA. Section 3 is devoted to describing the data used. The results and discussions are presented in Section 4, followed by the conclusion in Section 5.

2. Methods

This session provides brief overviews of the two statistical methods used in our analysis: singular spectrum analysis and the wavelet multiresolution analysis. For further details, the reader is referred to Ghil et al. [26] for singular spectrum analysis and to Mallat [27] for wavelet multiresolution analysis.

2.1. Singular spectrum analysis

The Singular Spectrum Analysis (SSA) is a well-known technique already used in a wide variety of disciplines. It allows a decomposition of a time series into three independent components (trend, oscillatory components, and noise). It consists of the following four steps [28]:

Step (1): Embedding of the original time series in a vector space of dimension M.

The starting point of the SSA procedure is to expand the time series $x(t)_{t=1,\ldots,N}$ into a vector space of dimension M ($1 < M < N/2$). It consists in transferring the one-dimensional time series $x(t)_{t=1,\ldots,N}$ into a multidimensional matrix $\boldsymbol{X}$ (called the trajectory matrix) as follows:

$$\boldsymbol{X}=\begin{pmatrix} x(1) & x(2) & \cdots & x(M) \\ x(2) & x(3) & \ldots & x(M+1) \\ \vdots & \vdots & \ddots & \vdots \\ x(N-M+1) & x(N-M+2) & \cdots & x(N) \end{pmatrix} \tag{1}$$

where M denotes the embedding dimension and N denotes the length of the initial time series.

Step (2): Construction of the $M \times M$ covariance matrix $\boldsymbol{C_X}$

The covariance matrix $\boldsymbol{C_X}$ $(M \times M)$ is calculated from the trajectory matrix $\boldsymbol{X}$ as follows:

$$\boldsymbol{C_X}=\frac{1}{N-M+1}\,\boldsymbol{X}^{\mathrm{T}}\boldsymbol{X} \tag{2}$$

Step (3): Determination of the eigenvalues and eigenvectors of the covariance matrix $\boldsymbol{C_X}$.

Once the covariance matrix $\boldsymbol{C_X}$ is computed, one determines its M eigenvalues λ_k $\{1 \le k \le M\}$ and their corresponding eigenvectors ρ_k. The eigenvalue λ_k gives the partial variance (PV) of the time series computed by Eq. (3). If we represent the eigenvalues λ_k in a diagram in decreasing order, one can often associated [28]: (1) an isolated eigenvalue to a trend in the time series, (2) a pair of nearby and isolated eigenvalues to a seasonal component in the time series, (3) the small eigenvalues to the noise affecting the time series.

$$\mathrm{PV}(k)=\frac{\lambda_k}{\sum_{k=1}^{M}\lambda_k} \tag{3}$$

Step (4): Reconstruction of time series.

From the computed eigenvectors ρ_k $(1 \le k \le M)$, the time series $x(t)_{t=1,\ldots,N}$ can be reconstructed into a new series of length N-M+1 as follows:

$$A_k(t)=\sum_{j=1}^{M} x(t+j-1)\,\rho_k(j), k=1,\ldots,M, t=1,\ldots,N-M+1 \tag{4}$$

By selecting a subset of κ eigenvectors, the reconstructed time series $x(t)_{t=1\ldots N-M+1}$ can be extended to the length N by summing its corresponding $A_k(t)$. The reconstructed series $R_\kappa(t)$ of length N will be called the reconstructed components (RCs) [26–28]:

$$R_\kappa(t)=\begin{cases} \dfrac{1}{t}\displaystyle\sum_{k\in\kappa}\sum_{j=1}^{t} A_k(t-j+1)\,\rho_k(j),\ 1 \le t \le M-1 \\ \dfrac{1}{M}\displaystyle\sum_{k\in\kappa}\sum_{j=1}^{M} A_k(t-j+1)\,\rho_k(j),\ M \le t \le N-M+1 \\ \dfrac{1}{N-t+1}\displaystyle\sum_{k\in\kappa}\sum_{j=t-N+M}^{M} A_k(t-j+1)\,\rho_k(j),\ N-M+2 \le t \le N \end{cases} \tag{5}$$

2.2. Wavelet multiresolution analysis

A wavelet ψ is a function of $L^2(R)$ with zero mean, which can be expanded/contracted and translated, forming a set of basic functions called wavelets on which the signal $X(t)$ is projected. The continuous wavelet transform (CWT) of the signal $X(t)$ can be expressed with the following equation [27,28]:

$$\mathrm{CWT}_{u,s}(t)=\int_{-\infty}^{+\infty} X(t)\,\overline{\psi}_{u,s}(t)\,\mathrm{d}t \tag{6}$$

$$\psi_{u,s}(t)=s^{-\frac{1}{2}}\,\psi\left(\frac{t-u}{s}\right) \text{with } s \in R_+^* \text{ and } u \in R \tag{7}$$

where u and s denote, respectively, the translation and scale factor, and $\overline{\psi}_{u,s}$ denotes the complex conjugate of the wavelet functions $\psi_{u,s}$.

The original signal can be reconstructed from its wavelet coefficients $\mathrm{CWT}_{u,s}$ by the inverse wavelet transforms [27]:

$$X(t)=\frac{1}{C_\psi}\int_0^{+\infty}\int_{-\infty}^{+\infty}\mathrm{CWT}_{u,s}(t)\,\psi_{u,s}(t)\,\mathrm{d}u\frac{\mathrm{d}s}{s^2} \tag{8}$$

$$C_\psi=\int_0^{+\infty}\frac{|\,\mathrm{FT}(\psi(t))|^2}{t}\,\mathrm{d}t \tag{9}$$

where C_ψ denotes the admissibility constant and FT is the Fourier Transform. For a successful inverse wavelet transform, the admissibility constant has to check the admissibility condition: $0<C_\psi<+\infty$.

By sampling the wavelet function ψ at discrete translations and scales, the discrete wavelet transform (DWT) is defined as follow [27,28]:

$$s=s_0^j \text{ and } u=k\,u_0\,s_0^j \text{ with } k,j\in Z, s_0>1 \text{ and } u_0>0$$

$$\psi_{j,k}(t)=s_0^{-\frac{j}{2}}\psi\left(\frac{t-ku_0s_0^j}{s_0^j}\right) \tag{10}$$

$$\mathrm{DWT}_{j,k}(t)=s_0^{-\frac{j}{2}}\int_{-\infty}^{+\infty}X(t)\,\overline{\psi}\left(s_0^{-j}t-ku_0\right)\,\mathrm{d}t \tag{11}$$

Varying scale and translation factors dyadically (i.e., powers of two) by selecting ($s_0 = 2$ and $u_0 = 1$), leads to a wavelet multiresolution analysis. The wavelet multiresolution analysis (WMA) [25] allows the computation of the wavelet coefficients $\mathrm{DWT}_{j,k}$ by decomposing the signal X on several scales and reconstructing it from the elements of this decomposition. At each scale, the original signal is decomposed into two signals: (i) the detail signal (representing its high frequencies), which allows to assess the seasonal variability of the signal, and (ii) the approximation signal (representing its low frequencies), which allows to identify the trend (velocity) of the signal. Fig. 1 illustrates the scheme of wavelet multiresolution analysis, in which a signal is decomposed into approximation and detail signals at successive levels.

3. Data used

3.1. DORIS data

The present study is based on the weekly combined residual coordinate time series (solution ids23wd04) of DORIS stations, available on the CDDIS data centre (ftp://cddis.gsfc.nasa.gov/pub/doris/products/stcd/) and the IGN data centre (ftp://doris.ensg.ign.fr/pub/doris/products/stcd/) in STCD (STation Coordinate Difference) format [29]. These data were processed by the IDS Combination Center [30] with the use of IGN CATREF (Combination and Analysis of Terrestrial Reference Frames) software package, aligned to ITRF2014 [31], and including data from fourteen DORIS satellites (SPOT-2/3/4/5, TOPEX/Poseidon, Envisat, Jason-1/2/3, Cryosat-2, HY-2A, Saral, Sentinel-3A/3B). More details on these data are provided in Moreaux et al. [32]. This study focussed on 45 well-observed stations (see Table 1 and Fig. 2); with a time span longer than four years and missing data (sequence of missing values) shorter than 8 weeks (see Table 2).

3.2. Global plate models

The DORIS horizontal velocities estimated by SSA and WMA are compared with six global plate models (REVEL 2000, GEODVEL 2010, ITRF2020, NUVEL 1A, MORVEL 2010, and GSRM 2.1) derived from the UNAVCO plate motion calculator website (https://www.unavco.org/software/geodetic-utilities/plate-motion-calculator/plate-motion-calculator.html). These global plate models depict an average of motion over larger spatial areas and long temporal scales.

REVEL 2000, GEODVEL 2010, and ITRF2020 are geodetic models based on data derived from space geodesy techniques, including VLBI, SLR, GNSS, and DORIS. REVEL 2000 (REcent VELocities) model [33] describes the relative motions of 19 tectonic plates and continental blocks. It is based primarily on GPS data collected between 1993 and 2000. GEODVEL 2010 (GEODesy VELocity) [34] is a plate model obtained by combining the solutions of the four space geodetic techniques: VLBI, SLR, DORIS, and GNSS. ITRF2020 (International Terrestrial Reference Frame) [35] uses as input data time series of station positions and Earth Orientation Parameters (EOPs) provided by the technique-specific analysis centers of VLBI, SLR, GNSS, and DORIS.

In contrast, NUVEL 1A and MORVEL 2010 are geophysical models based on geological data, such as seafloor magnetic anomalies and transform faults. NUVEL 1A (Northwestern University VELocity) model, developed by DeMets et al. [36], is a kinematic model that describes the relative motion of tectonic plates with respect to the Pacific plate, using geological data. MORVEL 2010 (Mid-Ocean Ridge VELocity) [37] model, based on updated geophysical and geodetic data, represents the motions of 25 tectonic plates, covering approximately 97% of the Earth's surface.

However, the GSRM 2.1 (Global Strain Rate Model) model [38] combines geodetic, geologic, and seismological data to constrain

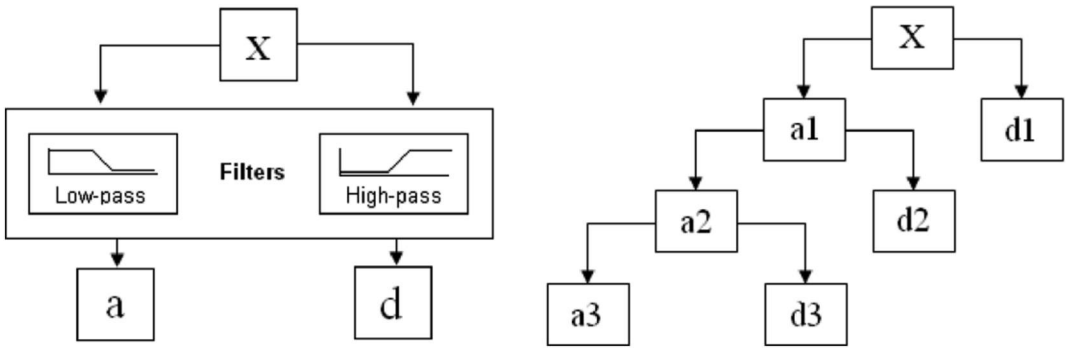


Fig. 1. Filtering process of wavelet multiresolution analysis: the original signal X passes through two complementary filters (low-pass and high-pass filters) and emerges as two signals: approximation (a) and detail (d). In right graph, three levels of decomposition are shown.

Table 1
DORIS stations selected in this study.

Site	Country	Acronym	Lat (deg)	Long (deg)	Tectonic plate
AMSTERDAM	France	AMVB	−37.80	77.57	Antarctic
ASCENSION	UK	ASEB	−7.92	−14.33	South American
BADARY	Russia	BADB	51.77	102.23	Eurasian
BELGRANO	Antarctica	BEMB	−77.87	−34.63	Antarctic
BETIO	Kiribati	BETB	1.35	172.92	Pacific
CACHOEIRA	Brazil	CADB	−22.68	−45.90	South American
COLD-BAY	USA	COBB	55.18	−162.70	North American
DIONYSOS	Greece	DIOB	38.08	23.93	Eurasian
DJIBOUTI	Djibouti	DJIB	11.53	42.85	African
EVEREST	Nepal	EVEB	27.95	86.82	Eurasian
FUTUNA	France	FUUB	−14.31	−178.12	Pacific
GRASSE	France	GR4B	43.75	6.92	Eurasian
GREENBELT	USA	GRFB	39.02	−76.83	North American
HARTEBEESTHOEK	South Africa	HBMB	−25.89	27.71	African
JIUFENG	China	JIWC	30.52	114.48	Eurasian
KAUAI	USA	KOLB	22.12	−159.67	Pacific
KITAB	Uzbekistan	KIVC	39.13	66.88	Eurasian
KOUROU	France	KRWB	5.10	−52.64	South American
KRASNOYARSK	Russia	KRBB	55.10	92.80	Eurasian
LA-REUNION	France	REUB	−21.21	55.57	African
LE-LAMENTIN	France	LAOB	14.60	−61.00	Caribbean
LIBREVILLE	Gabon	LICB	0.35	9.67	African
MAHE	Seychelles	MAIB	−4.68	55.53	African
MALE	Maldives	MALB	4.20	73.53	Indian
MANAGUA	Nicaragua	MNAC	12.15	−86.25	Caribbean
MANGILAO	USA	MLAC	13.43	144.80	Philippine
MANILLE	Philippines	MANB	14.52	121.03	Eurasian
MARION-SLAND	South Africa	MAUB	−46.88	37.85	Antarctic
METSAHOVI	Finland	MEUB	60.24	24.38	Eurasian
MIAMI	USA	MIAB	25.73	−80.17	North American
MOUNT-STROMLO	Australia	MSPB	−35.32	149.01	Australian
NOUMEA	France	NOXB	−22.23	166.48	Australian
NY-ALESUND	Norway	SPJB	78.92	11.93	Eurasian
OWENGA	New Zealand	OWFC	−44.03	−176.37	Pacific
PAPEETE	France	PAUB	−17.58	−149.61	Pacific
PONTA-DELGADA	Portugal	PDOC	37.75	−25.66	African
REYKJAVIK	Iceland	REZB	64.15	−21.91	North American
RIKITEA	France	RIMB	−23.13	−134.97	Pacific
RIO-GRANDE	Argentina	RIRB	−53.79	−67.75	South American
ST-HELENA	UK	HEMB	−15.94	−5.67	African
ST-JOHN-S	Canada	STKB	47.60	−52.68	North American
SYOWA	Antarctica	SYQB	−69.00	39.58	Antarctic
THULE	Denmark	THUB	76.54	−68.82	North American
TOULOUSE	France	TLSB	43.55	1.48	Eurasian
YARRAGADEE	Australia	YASB	−29.05	115.35	Australian

both rigid plate rotations and velocity gradient tensor fields in deforming regions.

4. Results and discussion

4.1. DORIS velocities derived by SSA and WMA

The SSA application, as previously shown, requires the prior selection of the embedding dimension (or window length) M, which must be smaller than half the length of the time series. This choice strongly influences SSA performance: a small M captures short-term oscillations but may miss slow variations, while a large M improves the extraction of trends and long-period components but can mix close frequencies. Selecting an appropriate M is therefore essential for effective component separation and accurate reconstruction. Hassani et al. [39] noted that when a time series contains a periodic component with an integer period, the window length M should be chosen proportional to that period to improve the extraction of the periodic signal. Also, Hassani et al. [40], based on the concept of signal–noise separability, recommended choosing M as the median of $\{1, \ldots, T\}$ for a time series of length T. Kols et al. [9], further, linked the choice of M to the noise level, using window lengths of 2, 3, and 4 years to achieve the most accurate results under different noise levels.

In this study, the optimal window length M is defined as the one that maximizes the Signal-to-Noise Ratio (SNR) and minimizes the reconstruction error quantified by the root mean square error (RMSE). To determine M, the time series is decomposed and reconstructed using several candidate window lengths: 1 year (52 weeks), 18 months (78 weeks), 2 years, 3 years, and the median of $\{1, \ldots, N\}$, where N is the length of the time series. For each candidate M, the SNR and RMSE are computed. The M that yields the highest SNR and the lowest RMSE is selected as optimal, ensuring accurate reconstruction of trends and periodic components while effectively separating signal from noise.

The results show that a window length of 52 weeks is optimal for all the analyzed time series. For instance, Fig. 3 shows that this window yields the highest SNR and the lowest RMSE for the East component of the AMSTERDAM (AMVB) station. In SSA theory, a large, isolated eigenvalue in the eigenvalue diagram indicates the presence of a dominant trend in the analyzed time series. Whereas, a pair of large, well-separated, and closely spaced eigenvalues is typically associated with a dominant seasonal (oscillatory) component. As an example, Fig. 4 presents the logarithm of the 52 eigenvalues derived from the SSA for the East component of the AMVB station. The first eigenvalue which is quite distinct from the other values, indicates a signature of a dominant trend represented by the reconstructed component RC1 (see Fig. 5) with a partial variance of 99.71% and a slope of about 9.83 ± 0.02 mm/yr. The second and third eigenvalues, which are well-detached from the first and the other remaining values, suggest the presence of an annual signal, represented by the reconstructed components RC2-3 (see Fig. 5), with a partial variance of 0.05%. For a window length of one year ($M = 52$ weeks), the trends estimated by SSA through the reconstructed components (RC1) explain more than 99% of the total variance in the horizontal components (North and East) for most stations.

In WMA theory, as previously stated, the trend displays the low-frequency components of the studied time series. It can be determined through the approximation signals resulting from the decomposition of the time series at several scales (resolutions). While, the periodic signals, representing the high-frequency components of the studied time series, are determined from the detailed signals.

Wavelet analysis relies on selecting an appropriate analysis function, which depends on the intended application [41,42]. Wavelet families differ in smoothness, compactness, symmetry, and suitability for various signal-processing tasks. The Meyer, Daubechies, Symlets, and Coiflets wavelets are among the most widely used because they offer complementary advantages depending on the desired balance between mathematical elegance, computational efficiency, and accuracy in representing trends or irregularities. The Meyer [41] wavelet is symmetric, infinitely smooth, and well-localized in frequency, making it efficient for spectral analysis (e.g., detecting periodic patterns or singularities). However, its non-compact support limits its

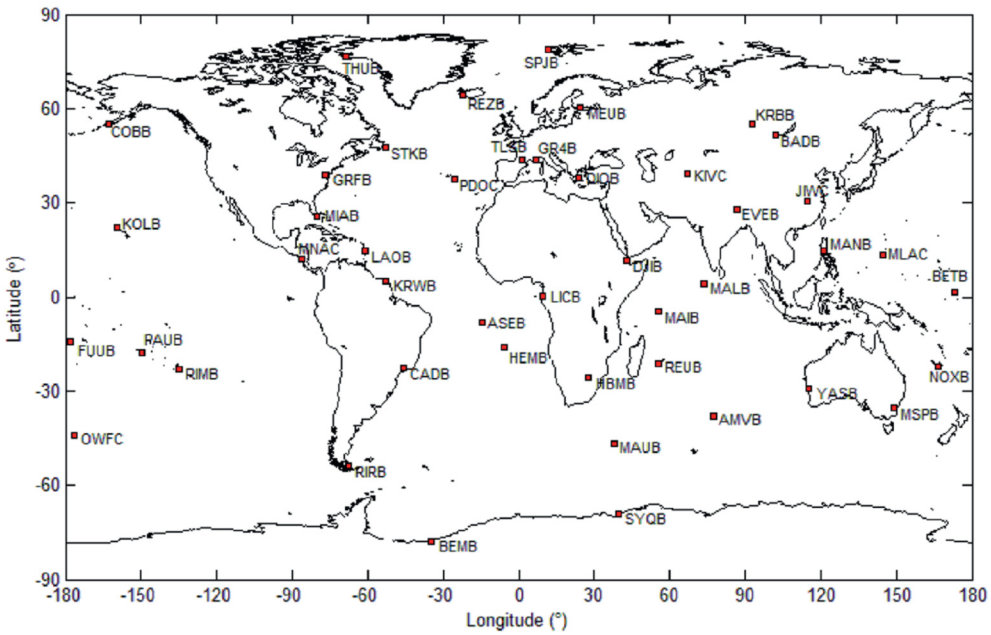


Fig. 2. Geographical distribution of the selected DORIS stations.

efficiency for short or highly noisy signals. Daubechies [43] wavelets have compact support and high vanishing moments, offering a robust balance between time and frequency resolution, which makes them widely used for trend extraction. Their main limitation is the lack of symmetry, which can introduce slight distortions in signals that require phase preservation. Symlets [27,43] are an improved version of Daubechies wavelets, sharing the same vanishing moments but with enhanced symmetry and compact support, which reduces reconstruction artifacts and makes them ideal for trend extraction, smooth denoising, and minimizing phase distortion. Coiflets [43,44] are more regular (smooth) and feature vanishing moments for both the wavelet and scaling functions, enabling accurate trend estimation and better detection of fine-scale variations.

In this study, the wavelet used for each time series (North, East, and Up) is selected as the one that yields the highest SNR, ensuring the most reliable extraction of the trend (or seasonal components). The trend and annual signals in the analyzed time series are determined, respectively, by the approximation signal at level 6 and the detail signal at level 5 of the decomposition. Table 3 shows that for the East component of the first 10 analyzed stations, the different wavelets (Meyer, Daubechies, Symlets, and Coiflets) provide nearly identical SNR values, with differences typically on the order of 0.1 - 0.01 dB. Fig. 6 illustrates, for the East component of the AMVB station, the sixth-level approximation (representing the trend) obtained using the Daubechies wavelet with six vanishing moments (db6), as well as the fifth-level detail (representing the annual signal) extracted using the Meyer wavelet. Fig. 7 presents the velocities estimated using SSA and WMA for the North, East, and Up components of the analyzed time series. The two methods yield strongly consistent velocity estimates. SSA, based in phase space, efficiently extracts periodic components across multiple temporal scales [45], whereas WMA, based in time–frequency space, accurately localizes trend changes through its approximation signals. Together, these approaches provide complementary and robust tools for analysing complex geodetic time series characterized by both oscillatory signals and trend shifts.

4.2. Assessment of DORIS horizontal velocities

As shown in Table 4, we can see that the differences between the horizontal velocities estimated from DORIS and those predicted by global plate models range from 0 to 4 mm/yr for most stations, but exceed 7 mm/yr for the six stations: AMSTERDAM (AMVB), DIONYSOS (DIOB), EVEREST (EVEB), MANAGUA (MNAC), MANGILAO (MLAC), and MANILLE (MANB). For these stations, Fig. 8 presents the East components along with their trends extracted by SSA. These large discrepancies can be attributed to the location of these six stations near plate boundaries and in active seismic zones (see Table 5). It should also be noted that the UNAVCO plate movement calculator assigns the AMSTERDAM site to the Australian tectonic plate, whereas its horizontal velocities (North and East) calculated by SSA and WMA are in good agreement with those calculated from Antarctic tectonic plate models, which differ significantly from those calculated from Australian tectonic plate models.

For the three sites DIONYSOS, EVEREST, and MANILLE, our results are consistent with those found in Moreaux et al. [46], which indicates that the horizontal velocities of these sites are greater than 10 mm/yr compared to global plate models (GEODVEL 2010 and MORVEL). As with the AMSTERDAM site, global plate models do not assign the DIONYSOS, EVEREST, and MANILLE sites to their respective tectonic plates. The DIONYSOS site is located on a moving local microplate (Aegean Sea Plate), whereas it is assigned to the Eurasian Plate by global models. The differences in horizontal velocities between DORIS and global models at the MANILLE site might be attributed to the fact that the movement rate of MANILLE could not be modeled by either the Sundaland or the Eurasian plates. As stated by Bird [47], MANILLE is situated on the Philippine Orogen. For the EVERSET site, along the southern border of Xizang, the velocity differences are largely attributed to the complex tectonic and seismic dynamics of this region, particularly the powerful magnitude 7.8 earthquake that struck Nepal and its surrounding areas on April 25, 2015. The MNAC site is characterized by significant tectonic activity, including the subduction of the Cocos plate beneath the North American and

Table 2
Data span, number of missing data (N.M.), percentage of missing data (P.M.) and largest gap length (L. Gaps) in the analyzed position time series.

Site	Acronym	Data span	N.M.	P.M. (%)	L. Gaps (weeks)
AMSTERDAM	AMVB	2010.7–2023.5	2	0.30	1
ASCENSION	ASEB	2010.6–2023.5	37	5.49	2
BADARY	BADB	2009.7–2018.1	1	0.23	1
BELGRANO	BEMB	2007.1–2023.5	16	1.87	1
BETIO	BETB	2013.7–2017.5	7	3.54	3
CACHOEIRA	CADB	2018.5–2023.5	38	14.39	4
COLD-BAY	COBB	2014.9–2023.5	0	0	0
DIONYSOS	DIOB	2006.5–2023.5	16	1.80	7
DJIBOUTI	DJIB	2012.7–2023.5	0	0	0
EVEREST	EVEB	2008.8–2023.5	32	4.15	3
FUTUNA	FUUB	2015.1–2019.0	0	0	0
GRASSE	GR4B	2019.6–2023.5	0	0	0
GREENBELT	GRFB	2019.4–2023.5	0	0	0
HARTEBEESTHOEK	HBMB	2011.0–2023.5	10	1.52	2
JIUFENG	JIWC	2019.1–2023.5	3	1.31	3
KAUAI	KOLB	2002.9–2023.0	5	0.48	2
KITAB	KIVC	2016.5–2023.5	3	0.82	2
KOUROU	KRWB	2018.8–2023.5	7	2.81	1
KRASNOYARSK	KRBB	2010.1–2018.1	3	0.71	2
LA-REUNION	REUB	2008.6–2019.3	9	1.61	5
LE-LAMENTIN	LAOB	2013.7–2023.5	23	4.50	7
LIBREVILLE	LICB	2009.3–2023.5	14	1.89	2
MAHE	MAIB	2018.9–2023.5	10	4.12	5
MALE	MALB	2013.4–2021.7	2	0.46	1
MANAGUA	MNAC	2018.9–2023.5	0	0	0
MANGILAO	MLAC	2018.3–2023.5	1	0.37	1
MANILLE	MANB	2011.8–2023.5	11	1.80	3
MARION-SLAND	MAUB	2014.7–2023.4	5	1.09	4
METSAHOVI	MEUB	2012.5–2023.5	0	0	0
MIAMI	MIAB	2017.9–2023.5	2	0.68	1
MOUNT-STROMLO	MSPB	2007.0–2023.5	4	0.47	4
NOUMEA	NOXB	2011.7–2022.1	12	2.20	2
NY-ALESUND	SPJB	2005.0–2018.8	11	1.52	1
OWENGA	OWFC	2016.2–2022.6	2	0.6	1
PAPEETE	PAUB	2009.9–2021.8	5	0.81	2
PONTA-DELGADA	PDOC	2016.0–2023.5	1	0.26	1
REYKJAVIK	REZB	2012.4–2020.7	10	2.30	6
RIKITEA	RIMB	2017.2–2023.5	13	3.92	8
RIO-GRANDE	RIRB	2012.3–2018.8	1	0.29	1
ST-HELENA	HEMB	2019.4–2023.5	0	0	0
ST-JOHN-S	STKB	2013.7–2019.5	0	0	0
SYOWA	SYQB	2014.4–2021.2	1	0.28	1
THULE	THUB	2008.1–2023.5	4	0.50	1
TOULOUSE	TLSB	2007.5–2023.5	0	0	0
YARRAGADEE	YASB	2004.0–2023.5	0	0	0

Caribbean plates, which leads to earthquakes, volcanism, and complex crustal deformation. The velocity discrepancies probably reflect the localized strain and motion associated with this active plate boundary, which global models may only represent in a smoothed long-term average. The MLAC site is located in the western Pacific Ocean, likely on or near the island of Guam, which is part of the Mariana Arc system. This region is characterized by significant tectonic activity due to the subduction of the Pacific Plate beneath the Philippine Sea Plate.

We also observed a higher discrepancy between DORIS estimates and those of global plate models for the East component of CACHOEIRA (CADB) station; this can be probably linked to the high orbit inclination of some DORIS satellites as SPOTs (98° inclination), Envisat (98.6°), Cryosat-2 (92°), HY-2A (99°) and Saral (98.5°) [12]. For the DORIS system, the East component is generally less well determined than the other two (North and Vertical); most DORIS satellites have high inclinations, resulting in roughly North-south orientation of the satellite passes over the stations. This pass geometry implies a poor determination of the East station coordinates [15]. Another explanation suggests that the

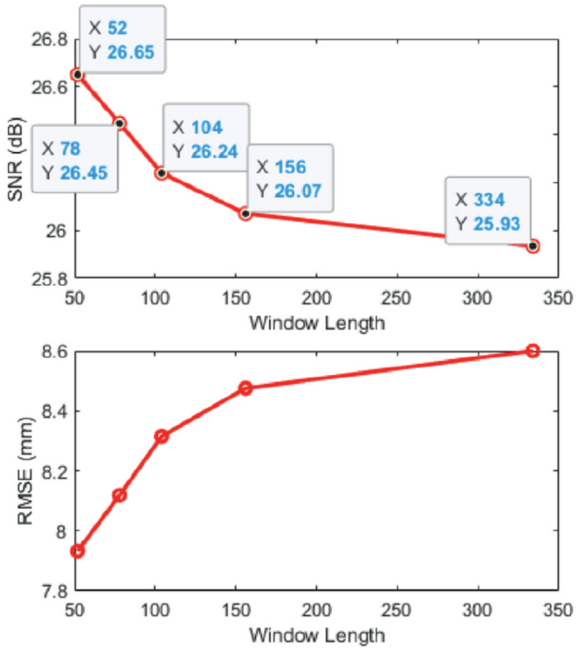


Fig. 3. Signal-to-noise ratio (SNR) and reconstruction error (RMSE) obtained for different analysis window lengths.

position and velocity solutions of the CADB station may be influenced by errors associated with the South Atlantic Anomaly (SAA), which affects the on-board Ultra Stable Oscillator (USO) of DORIS/SPOT-5, resulting in a significant deterioration of their positioning since 2007 [12,48], particularly as this station is situated at the center of the SAA. Furthermore, these results are consistent with those found in Khelifa [12], which state that the East component of the CADB station is characterized by a higher noise level.

4.3. Assessment of DORIS vertical velocities

To validate the DORIS vertical velocities, we estimated the vertical velocities of collocated GPS stations over the same observation period using WMA. The considered GPS time series (see Table 6) are processed by the Nevada Geodetic Laboratory (NGL), referenced to the ITRF2014 coordinate system, expressed in

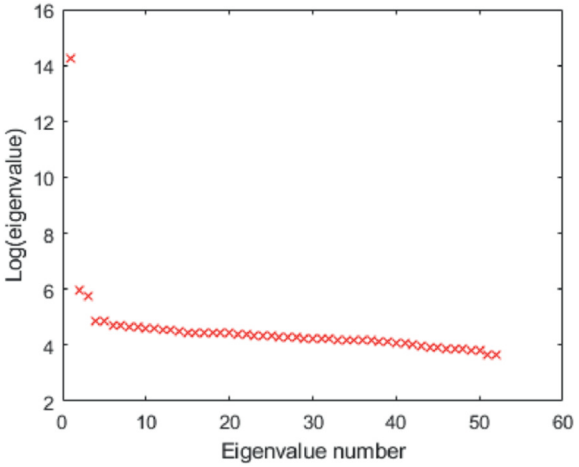


Fig. 4. Diagrams of the 52 eigenvalues for the East component of the AMVB station.

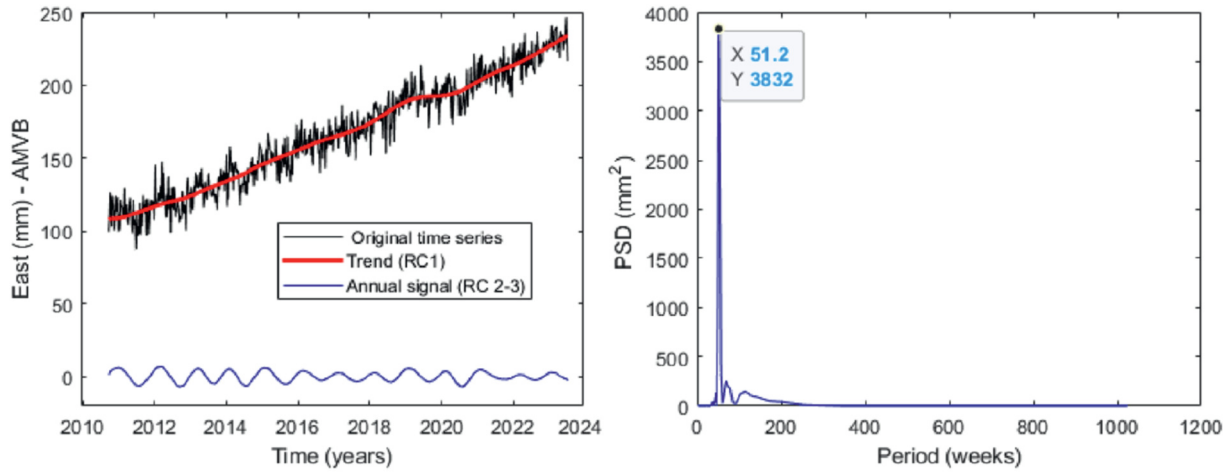


Fig. 5. East component of the AMVB station with its trend and annual signal extracted by SSA (left), and the periodogram (PSD) of the annual signal (RC2-3) (right), showing the periodicity of 1 year (51.2 weeks).

the local frame (North, East, and Up) and available at (https://geodesy.unr.edu/NGLStationPages/stations/). The NGL data include information from the International GNSS Service (IGS) and various other geodetic networks from different countries. More details on these data can be found in Blewitt et al. [49].

The DORIS vertical velocities are compared with those of GPS at 26 co-located sites, over the same time span. As shown in Fig. 9, it can be seen that the differences are approximately 1 mm/yr at more than 77% of the sites (i.e., 20 sites), while they are approximately 2 mm/yr for the six sites (GRASSE, KOUROU, LE-LAMENTIN, MANAGUA, PONTA-DELGADA, RIO-GRANDE). The differences between DORIS and GPS vertical velocities at these sites, as seen in Table 6, do not appear to depend on the distance or height between the DORIS and GPS stations. Similar to the comparison of horizontal velocities, these differences can be explained by the fact that these sites are located at plate boundaries or in active seismic areas. They may also arise from subtle discontinuities in the analyzed DORIS or GPS position time series, induced by earthquakes or by technical events affecting beacons or antennas.

Additionally, system-specific error sources contribute to these differences. GPS is primarily affected by ionospheric and tropospheric delays, satellite and receiver clock instabilities, antenna phase center, and multipath effects. DORIS, by contrast, is sensitive to noise at low elevation angles [50], mismodeling of solar radiation pressure [51], and ultra-stable oscillator instabilities induced by the South Atlantic Anomaly [48,52]. Beyond these system-specific limitations, geophysical processes such as Glacial Isostatic Adjustment (GIA), atmospheric loading, hydrological effects (e.g., soil moisture and snow accumulation), local ground instabilities, and the Earth's viscoelastic response can produce vertical deformation signals that significantly affect geodetic measurements. On the other hand, recent studies [53,54] indicate that, despite advances in modeling and correction strategies, these error sources continue to constrain the precision of both systems, particularly under conditions of increased solar activity and pronounced environmental variability.

Furthermore, the high-latitude sites METSAHOVI (60.24°), THULE (76.54°), and NY-ALESUND (78.92°) exhibit high vertical velocities of around 4.6 mm/yr, 7.2 mm/yr, and 8 mm/yr for GPS, and 5.1 mm/yr, 7.3 mm/yr, and 6.7 mm/yr for DORIS, respectively. These uplift rates are generally attributed to Glacial Isostatic Adjustment (GIA) associated with postglacial rebound. However,

Table 3
SNR (dB) for the East component of the first 10 analyzed stations using different wavelets.

Station	Meyer	Daubechies		Symlets		Coiflets		Chosen wavelet
		db4	db6	sym4	sym6	coif2	coif3	
AMVB	25.45	25.38	25.49	25.44	25.45	25.45	25.44	db6
ASEB	20.76	20.81	20.79	20.84	20.83	20.84	20.83	coif2
BADB	33.92	34.10	34.18	34.13	34.21	34.13	34.18	sym6
BEMB	27.90	27.96	27.95	27.99	27.98	27.98	27.98	sym4
BETB	7.98	40.34	40.55	40.78	40.76	40.82	40.69	coif2
CADB	19.89	19.57	19.78	19.86	19.98	20.00	19.98	coif2
COBB	26.69	26.63	26.81	27.00	26.97	26.97	26.98	sym4
DIOB	22.09	22.08	22.08	22.09	22.10	22.09	22.10	sym6
DJIB	37.17	37.56	37.50	37.47	37.49	37.48	37.51	db4
EVEB	34.62	34.62	34.72	34.55	34.60	34.57	34.60	db6

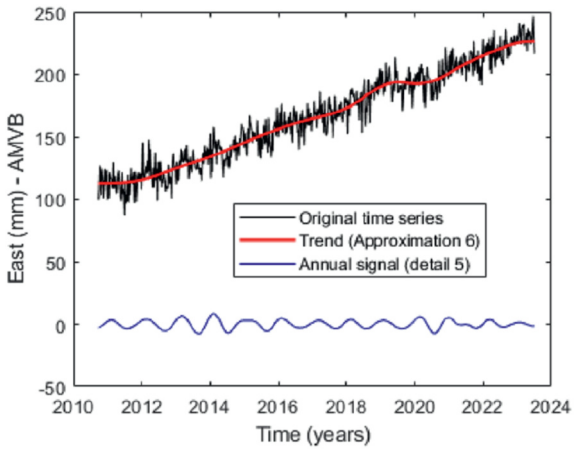


Fig. 6. East component of the AMVB station with its trend and annual signal extracted by WMA.

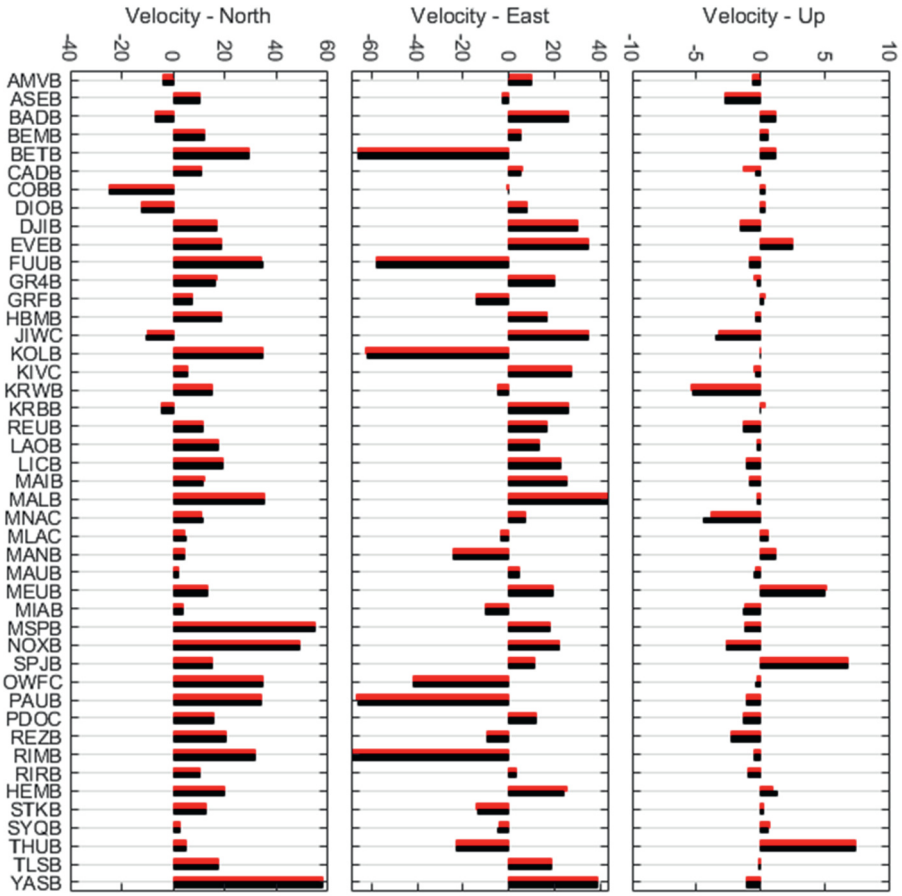


Fig. 7. Velocities (mm/yr) in the components (North, East, and Up) obtained by SSA (red) and WMA (black).

Table 4
Horizontal velocities estimated by SSA, WMA, and those calculated from plate tectonic models (GSRM 2.1, ITRF2020, GEODVEL 2010, REVEL 2000, MORVEL 2010, and NUVEL 1A) using UNAVCO plate motion calculator.

		Horizontal velocities (mm/yr)							
		SSA	WMA	GEODVEL	MORVEL	ITRF2020	NUVEL 1A	REVEL	GSRM 2.1
African plate									
DJIB	North	17.06 ± 0.03	17.03 ± 0.03	—	—	—	18.36	—	17.64
	East	30.50 ± 0.03	30.52 ± 0.03	—	—	—	26.36	—	25.84
HBMB	North	18.34 ± 0.02	18.34 ± 0.02	—	—	—	20.13	—	19.78
	East	16.95 ± 0.03	17.02 ± 0.03	—	—	—	20.72	—	19.38
HEMB	North	19.66 ± 0.05	19.57 ± 0.08	—	—	—	19.10	—	19.60
	East	24.38 ± 0.08	25.25 ± 0.05	—	—	—	26.14	—	24.99
LICB	North	19.37 ± 0.02	19.41 ± 0.01	—	—	—	20.44	—	20.55
	East	23.01 ± 0.02	22.99 ± 0.03	—	—	—	25.00	—	24.22
MAIB	North	11.77 ± 0.07	11.79 ± 0.07	—	—	—	15.87	—	14.89
	East	25.34 ± 0.14	25.25 ± 0.15	—	—	—	23.87	—	22.99
PDOC	North	15.80 ± 0.03	15.87 ± 0.03	—	—	—	15.34	—	16.28
	East	12.07 ± 0.03	12.00 ± 0.04	—	—	—	11.47	—	11.54
REUB	North	11.71 ± 0.01	11.75 ± 0.01	—	—	—	15.86	—	14.88
	East	16.87 ± 0.02	17.02 ± 0.02	—	—	—	18.63	—	17.49
Antarctic plate									
AMVB	North	−4.21 ± 0.02	−4.24 ± 0.02	37.41	37.19	37.04	41.74	36.21	39.08
	East	9.83 ± 0.02	9.70 ± 0.03	56.80	58.40	57.58	57.71	58.54	58.15
BEMB	North	12.18 ± 0.01	12.19 ± 0.01	12.15	11.46	12.63	11.87	12.92	12.89
	East	5.63 ± 0.03	5.61 ± 0.03	3.87	6.62	3.09	6.79	2.43	5.74
MAUB	North	1.93 ± 0.05	1.95 ± 0.05	3.13	4.71	2.51	5.34	1.86	4.85
	East	4.51 ± 0.03	4.67 ± 0.04	5.79	9.65	5.29	8.35	5.22	6.70
SYQB	North	2.30 ± 0.02	2.49 ± 0.02	2.77	4.38	2.13	5.01	1.46	4.48
	East	−4.51 ± 0.04	−4.35 ± 0.05	−3.52	−0.86	−4.14	−1.69	−4.44	−3.21
Australian plate									
MSPB	North	54.99 ± 0.02	55.10 ± 0.02	54.42	54.43	54.77	53.71	53.47	54.79
	East	18.00 ± 0.01	18.05 ± 0.01	18.20	19.94	18.99	17.76	20.91	18.76

(*continued on next page*)

Table 4 (*continued*)

		Horizontal velocities (mm/yr)							
		SSA	WMA	GEODVEL	MORVEL	ITRF2020	NUVEL 1A	REVEL	GSRM 2.1
NOXB	North	48.72 ± 0.05	48.73 ± 0.04	45.57	45.65	46.06	43.45	44.95	45.43
	East	22.46 ± 0.04	22.32 ± 0.04	20.70	22.61	21.41	21.70	23.61	21.77
YASB	North	58.10 ± 0.02	58.14 ± 0.01	57.06	56.94	57.07	59.13	55.75	58.27
	East	39.17 ± 0.01	39.21 ± 0.01	38.60	40.42	39.43	38.98	41.06	39.65
Caribbean plate									
LAOB	North	17.46 ± 0.02	17.41 ± 0.03	—	13.65	15.72	11.46	11.91	14.79
	East	13.14 ± 0.07	13.21 ± 0.08	—	12.22	11.32	5.17	12.73	13.96
MNAC	North	11.34 ± 0.06	11.12 ± 0.09	—	2.89	−3.51	2.54	1.92	4.53
	East	7.35 ± 0.03	7.28 ± 0.04	—	12.54	12.69	5.37	13.12	14.11
Eurasian plate									
BADB	North	−7.05 ± 0.02	−7.12 ± 0.02	−6.64	−7.83	−5.96	−9.33	−6.22	−5.18
	East	26.48 ± 0.03	26.45 ± 0.04	25.59	22.76	26.27	23.11	25.84	28.13
DIOB	North	−12.09 ± 0.01	−12.10 ± 0.01	12.87	12.40	13.59	11.41	12.16	14.90
	East	8.28 ± 0.01	8.28 ± 0.01	23.88	21.20	23.82	23.16	24.66	24.68
EVEB	North	18.71 ± 0.08	18.79 ± 0.09	−2.55	−3.76	−1.73	−5.40	−2.36	−0.67
	East	34.66 ± 0.06	34.60 ± 0.07	27.64	23.92	28.14	25.06	28.50	29.90
GR4B	North	16.34 ± 0.05	16.88 ± 0.06	15.07	14.95	15.59	14.39	14.22	16.70
	East	20.28 ± 0.04	20.02 ± 0.04	20.22	17.97	19.98	20.09	21.03	20.45
JIWC	North	−10.47 ± 0.09	−10.17 ± 0.10	−9.58	−10.69	−9.03	−12.01	−9.00	−8.52
	East	34.95 ± 0.11	34.99 ± 0.16	26.23	22.31	26.90	23.05	27.11	28.86
KIVC	North	5.36 ± 0.02	5.38 ± 0.03	2.98	1.88	3.88	0.24	2.85	5.20
	East	27.41 ± 0.02	27.39 ± 0.02	27.67	24.67	28.00	25.98	28.22	29.49
KRBB	North	−4.74 ± 0.02	−4.72 ± 0.02	−4.17	−5.38	−3.40	−6.98	−3.89	−2.44
	East	26.04 ± 0.03	26.06 ± 0.04	25.75	23.28	26.34	23.74	25.86	28.05
MANB	North	4.20 ± 0.02	4.26 ± 0.02	−10.98	−12.03	−10.52	−13.23	−10.32	−10.16
	East	−24.47 ± 0.04	−24.42 ± 0.05	25.10	20.82	25.63	21.93	26.33	27.43
MEUB	North	13.25 ± 0.03	13.28 ± 0.03	12.78	12.30	13.50	11.30	12.07	14.82
	East	19.63 ± 0.02	19.63 ± 0.01	19.68	18.52	19.38	20.39	19.89	19.69
SPJB	North	15.30 ± 0.03	15.33 ± 0.03	14.53	14.30	15.11	13.61	13.71	16.28
	East	11.48 ± 0.02	11.52 ± 0.02	10.85	11.19	10.25	12.95	10.72	9.77
TLSB	North	17.28 ± 0.01	17.31 ± 0.01	15.50	15.49	15.95	15.09	14.62	16.96
	East	18.97 ± 0.02	18.94 ± 0.01	19.26	17.00	18.99	19.16	20.14	19.40
Indian plate									
MALB	North	35.17 ± 0.04	35.11 ± 0.04	33.12	37.59	33.60	40.72	31.87	36.32
	East	43.92 ± 0.04	43.98 ± 0.04	44.48	45.86	43.78	42.30	43.12	44.76
North American plate									
COBB	North	−24.65 ± 0.12	−24.62 ± 0.12	−21.06	−22.88	−20.03	−22.36	−21.97	−23.89
	East	−0.35 ± 0.17	−0.58 ± 0.19	−4.55	−3.74	−5.65	−4.85	−2.54	−3.29
GRFB	North	7.29 ± 0.03	7.61 ± 0.05	3.19	1.54	3.33	3.62	0.87	2.94
	East	−14.07 ± 0.02	−14.01 ± 0.03	−14.34	−15.99	−15.11	−14.99	−14.58	−14.44
MIAB	North	3.72 ± 0.03	3.76 ± 0.04	1.94	0.19	2.14	2.30	−0.42	1.52
	East	−10.32 ± 0.04	−9.99 ± 0.07	−10.38	−11.76	−11.59	−10.76	−10.39	−9.66
REZB	North	20.52 ± 0.03	20.51 ± 0.04	19.29	19.73	18.54	20.63	18.57	21.45
	East	−9.60 ± 0.03	−9.59 ± 0.04	−9.21	−11.63	−9.37	−9.47	−11.17	−9.91
STKB	North	12.69 ± 0.03	12.88 ± 0.03	11.65	10.84	11.36	12.59	9.83	12.57
	East	−13.72 ± 0.02	−13.95 ± 0.03	−14.20	−16.35	−14.70	−14.81	−15.21	−14.73
THUB	North	5.01 ± 0.02	4.98 ± 0.02	6.12	4.73	6.12	6.74	3.93	6.27
	East	−22.82 ± 0.01	−22.88 ± 0.01	−20.38	−22.42	−19.80	−21.55	−21.35	−22.63
Pacific plate									
BETB	North	29.64 ± 0.13	29.21 ± 0.08	30.01	27.41	29.79	29.45	27.54	29.83
	East	−66.26 ± 0.07	−65.69 ± 0.20	−68.04	−65.27	−66.97	−63.89	−66.05	−66.14
FUUB	North	34.44 ± 0.06	33.81 ± 0.11	32.18	29.72	31.96	31.16	29.66	31.80
	East	−57.86 ± 0.08	−58.11 ± 0.11	−62.77	−59.82	−61.74	−59.52	−60.90	−61.28
KOLB	North	34.79 ± 0.02	34.85 ± 0.01	34.15	32.14	33.94	32.28	31.70	33.38
	East	−62.07 ± 0.02	−62.25 ± 0.02	−62.99	−61.07	−62.02	−58.31	−61.40	−60.85
OWFC	North	34.50 ± 0.06	34.44 ± 0.04	32.47	30.04	32.25	31.37	29.94	32.05
	East	−41.88 ± 0.04	−41.94 ± 0.05	−41.49	−38.71	−40.73	−40.50	−40.13	−41.03
PAUB	North	34.06 ± 0.02	34.08 ± 0.02	33.75	32.08	33.54	31.49	31.45	32.80
	East	−66.25 ± 0.04	−66.41 ± 0.03	−66.12	−62.84	−65.07	−62.83	−63.92	−64.63
RIMB	North	31.74 ± 0.04	31.70 ± 0.04	31.31	30.22	31.14	28.62	29.36	30.15
	East	−68.97 ± 0.10	−68.59 ± 0.15	−67.59	−64.08	−66.56	−64.38	−65.15	−66.14
Philippine plate									
MLAC	North	4.78 ± 0.10	4.49 ± 0.12	—	4.71	—	−0.22	5.82	8.11
	East	−3.74 ± 0.12	−3.49 ± 0.17	—	−54.71	—	−41.79	−55.48	−54.78
South American plate									
ASEB	North	10.51 ± 0.03	10.51 ± 0.03	10.68	11.08	10.45	12.92	9.13	12.92
	East	−2.76 ± 0.05	−2.78 ± 0.06	−4.81	−4.85	−5.58	−3.73	−5.86	−3.73
CADB	North	10.97 ± 0.07	10.94 ± 0.09	11.93	10.30	11.86	11.47	10.66	12.63
	East	5.12 ± 0.13	5.67 ± 0.15	−3.41	−2.63	−4.23	−4.23	−4.73	−1.50
KRWB	North	15.03 ± 0.02	14.88 ± 0.05	11.74	9.72	11.71	11.13	10.58	12.07
	East	−4.50 ± 0.13	−4.56 ± 0.16	−4.30	−5.14	−5.02	−5.85	−5.26	−3.82
RIRB	North	10.45 ± 0.03	10.44 ± 0.04	10.69	7.91	10.75	9.77	9.84	10.18
	East	3.36 ± 0.02	3.11 ± 0.04	1.87	3.59	1.15	1.88	0.20	4.87

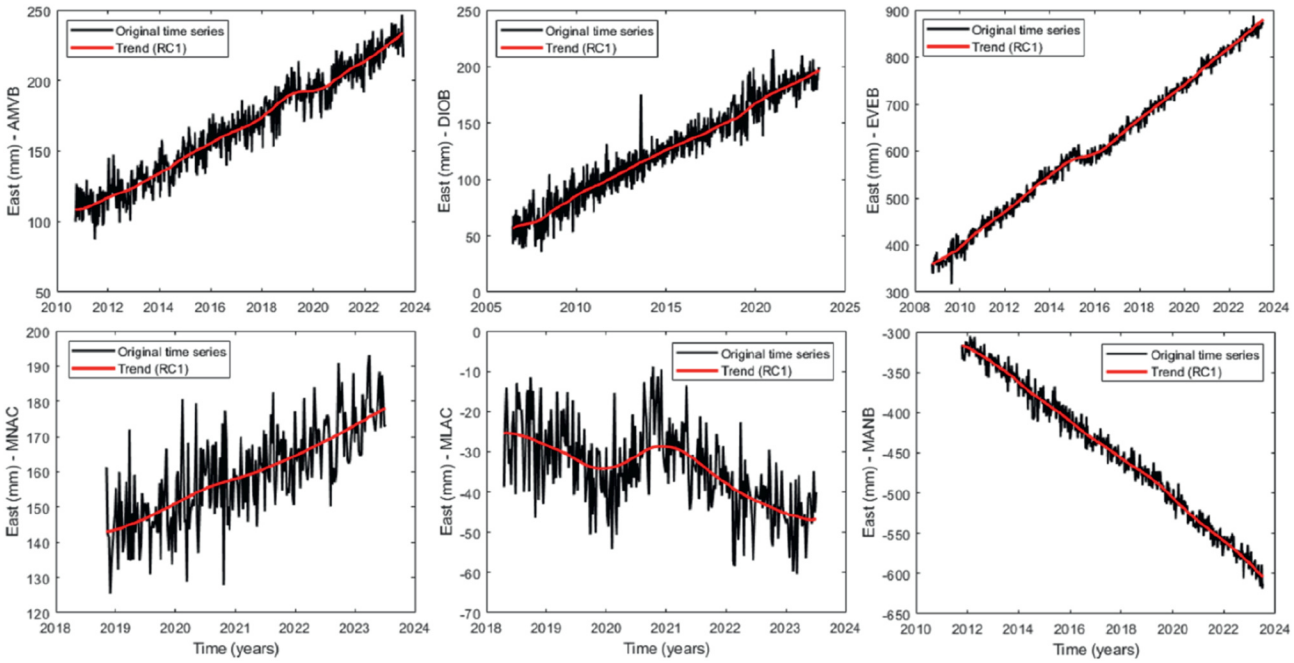


Fig. 8. East components with their trends extracted by SSA for the six stations: AMSTERDAM (AMVB), DIONYSOS (DIOB), EVEREST (EVEB), MANAGUA (MNAC), MANGILAO (MLAC), and MANILLE (MANB).

Table 5
The last 5 seismic events for the stations: AMVB, DIOB, EVEB, MNAC, MLAC, and MANB.

Station	Location	Earthquakes near the station
AMSTERDAM (AMVB)	Near the boundary of the Antarctic and Australian plates.	2013-10-04 17:26, mag: 6.4, distance: 114 km 2014-11-03 08:48, mag: 6.3, distance: 483 km 2015-03-06 08:22, mag: 6, distance: 470 km 2015-08-13 10:39, mag: 6, distance: 97 km 2020-04-12 06:57, mag: 6.1, distance: 95 km
DIONYSOS (DIOB)	Near the boundary of the Aegean sea microplate and the Eurasian plates.	2020-05-02 12:51, mag: 6.5, distance: 462 km 2020-10-30 11:51, mag: 7, distance: 251 km 2021-03-03 10:16, mag: 6.3, distance: 241 km 2021-09-27 06:17, mag: 6, distance: 337 km 2021-10-12 09:24, mag: 6.4, distance: 383 km
EVEREST (EVEB)	Near the boundary of the Eurasian and the Indian plates.	2011-09-18 12:40, mag: 6.9, distance: 134 km 2015-04-25 06:11, mag: 7.8, distance: 207 km 2015-04-25 06:45, mag: 6.6, distance: 198 km 2015-04-26 07:09, mag: 6.7, distance: 81 km 2015-05-12 07:05, mag: 7.3, distance: 75 km
MANAGUA (MNAC)	Near the boundary of the Caribbean and Cocos plates.	2021-05-12 08:45, mag: 6, distance: 450 km 2021-09-22 09:57, mag: 6.5, distance: 176 km 2021-11-09 06:25, mag: 6.3, distance: 108 km 2022-01-06 16:25, mag: 6.1, distance: 100 km 2022-04-21 07:42, mag: 6.6, distance: 102 km
MANGILAO (MLAC)	Near the boundary of the Eurasian and the Philippine plates.	2018-08-28 22:35, mag: 6.4, distance: 434 km 2022-02-13 20:29, mag: 6, distance: 192 km
MANILLE (MANB)	Near the boundary of the Eurasian and the Philippine plates.	2022-05-21 21:50, mag: 6.1, distance: 71 km 2022-07-27 00:43, mag: 7, distance: 333 km 2022-10-25 14:59, mag: 6.4, distance: 349 km 2023-02-15 18:10, mag: 6.1, distance: 393 km 2023-04-04 12:54, mag: 6.2, distance: 494 km

the ICE-6G (VM5a) model [55] predicts vertical velocities of only 1 mm/yr, which is significantly lower than the observed 7 mm/yr at both THULE and NY-ALESUND. This discrepancy can be mainly explained by the elastic response to ongoing ice mass loss, which is further intensified by regional and seasonal effects, such as local glacier dynamics and tectonic activity.

Table 6
GPS-DORIS co-located stations.

Site	Acronym DORIS	Acronym GPS	Common data span	Distance (m)	Height DORIS (m)	Height GPS (m)
BADARY	BADB	BADG	2009.7–2018.1	4.28	813.6	811.4
BETIO	BETB	KIRI	2013.7–2017.5	17.96	37.5	36.2
DIONYSOS	DIOB	DYNG	2011.3–2023.5	41.18	513.6	510.6
FUTUNA	FUUB	FTNA	2015.1–2019.0	6.19	85.8	84.9
GRASSE	GR4B	GRAS	2019.6–2023.5	53.75	1324.8	1319.3
GREENBELT	GRFB	GODE	2019.4–2023.5	206.02	20.3	14.5
HARTEBEESTHOEK	HBMB	HARB	2011.0–2023.5	24.89	1560.1	1558.1
KAUAI	KOLB	KOKB	2002.9–2023.0	358.80	1168	1167.4
KOUROU	KRWB	KOUG	2018.8–2023.5	16.90	109.9	107.3
LA-REUNION	REUB	REUN	2008.6–2019.3	16.18	1561.9	1558.4
LE-LAMENTIN	LAOB	LMMF	2013.7–2023.5	24.36	−29.0	−27.1
LIBREVILLE	LICB	NKLG	2009.3–2023.5	10.88	35.0	31.5
MANAGUA	MNAC	MANA	2018.9–2023.5	102.76	78.8	71.0
METSAHOVI	MEUB	METS	2012.5–2023.5	2797.10	63.8	63.8
MOUNT-STROMLO	MSPB	STR2	2007.0–2023.5	17.18	805.5	802.5
NY-ALESUND	SPJB	NYA1	2005.0–2018.8	1581.04	53.2	84.0
PAPEETE	PAUB	THTI	2009.9–2021.8	6.87	100.5	98.1
PONTA-DELGADA	PDOC	PDEL	2016.0–2023.5	6.20	111.1	110.6
REYKJAVIK	REZB	REYK	2012.4–2020.7	2380.52	84.3	93.1
RIO-GRANDE	RIRB	RIO2	2012.3–2018.8	40.80	33.7	32.0
ST-HELENA	HEMB	STHL	2019.4–2023.5	20.04	455.8	453.2
ST-JOHN-S	STKB	STJO	2013.7–2019.5	25.79	153.5	152.8
SYOWA	SYQB	SYOG	2014.4–2021.2	312.21	43.3	50.0
THULE	THUB	THU3	2008.1–2019.0	61.10	40.6	36.1
TOULOUSE	TLSB	TLSE	2007.5–2023.5	1272.02	212.5	207.1
YARRAGADEE	YASB	YAR2	2004.0–2023.5	48.08	243.9	241.3

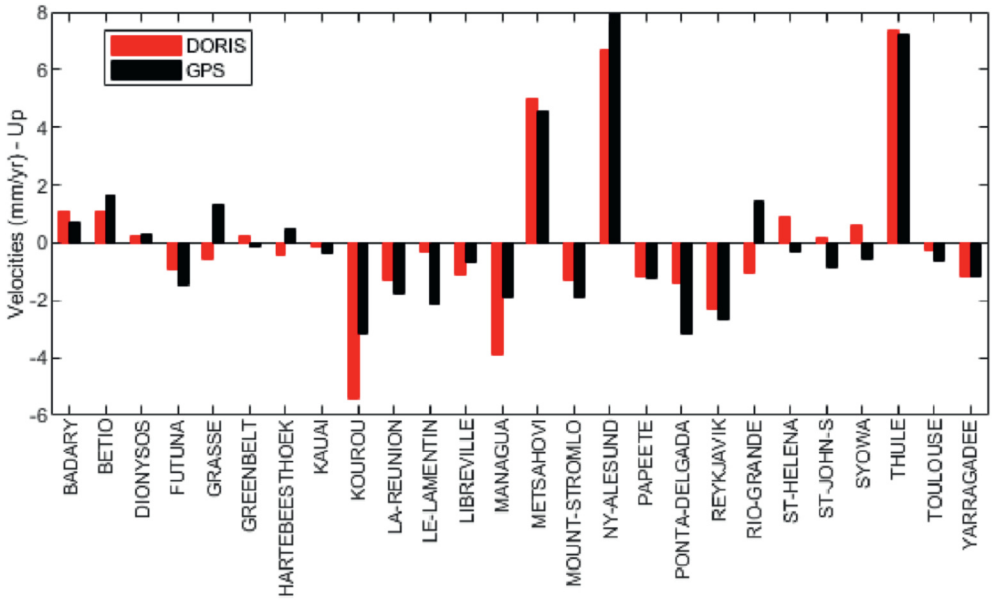


Fig. 9. Vertical velocities of the 26 GPS–DORIS co-located stations.

5. Conclusions

In this study, we assessed the horizontal and vertical velocities of 45 well-distributed DORIS sites worldwide, from using weekly time series of combined residual coordinates (solution ids23wd04) from well-observed stations, covering the time period from 2003.0 to 2023.5. The velocities were estimated using the SSA and WMA methods, which enable the direct and rapid extraction of the trend from the time series.

The SSA successfully extracted and quantified the trends found in the analyzed time series; they represent more than 99% of the overall signal for the horizontal components. The WMA results are consistent with those obtained by SAA for the three components (North, East, and Up) of the analyzed time series.

The horizontal velocities of the DORIS sites were compared with global plate models (REVEL 2000, GEODVEL 2010, ITRF2020, NUVEL 1A, MORVEL 2010, and GSRM 2.1) using the UNAVCO plate motion calculator. For most sites, DORIS horizontal velocities differ from global plate models by less than 1–4 mm/yr. However, for the six sites: AMSTERDAM (AMVB), DIONYSOS (DIOB), EVEREST (EVEB), MANAGUA (MNAC), MANGILAO (MLAC), and MANILA (MANB), the horizontal velocities differ from these models by more than 7 mm/yr. These higher disparities can be attributed to the fact that these sites are located in regions of seismic activity and close to plate boundaries. This study also reveals that the AMSTERDAM site is assigned to the Australian tectonic plate according to the UNAVCO plate motion calculator. However, their horizontal velocities estimated by SSA and WMA differ significantly from those calculated

from models of this plate, but are in good agreement with those obtained from models of Antarctic tectonic plates. The results also show a clear difference between the East velocity of the CADB station and that of the global plate models. This component exhibits an increasing trend of approximately 5 mm/yr, which contrasts with a decreasing trend in global models. This difference can be explained by the fact that the East component in the DORIS system is generally more perturbed than the North and Up components, which is related to the inclination of the DORIS satellite orbits.

The DORIS vertical velocities are substantially lower than horizontal ones and are close to those derived from co-located GPS stations, with values ranging from −3 mm/yr to 2 mm/yr. However, the high latitude stations THULE (76.54°) and NY-ALESUND (78.92°) exhibit high velocities of about 7 mm/yr; mainly due to the elastic response to ongoing ice mass loss, amplified by regional and seasonal effects such as local glacier dynamics and tectonic activity.

CRediT authorship contribution statement

Sofiane Khelifa: Writing – review & editing, Writing – original draft, Visualization, Validation, Supervision, Software, Project administration, Methodology, Investigation, Formal analysis, Conceptualization. **Saddam Housseyn Allal:** Writing – review & editing, Validation, Methodology. **Hicham Dekkiche:** Writing – review & editing, Validation, Methodology.

Data availability

The DORIS time series are available for download and for visualization at http://ids-doris.org/webservice. The GPS time series are freely provided at https://geodesy.unr.edu/NGLStation Pages/stations/. The velocities of the plate tectonic models are computed from the UNAVCO plate motion calculator (https://www.unavco.org/software/geodetic-utilities/plate-motion-calculator/plate-motion-calculator.html).

Declaration of competing interest

The authors declare that there is no conflicts of interest.

References

[1] J. Saunier, The DORIS network: advances achieved in the last fifteen years, Adv. Space Res. 72 (1) (2023) 3–22, https://doi.org/10.1016/j.asr.2022.07.016.
[2] G. Guergana, S. Tzvetan, Global navigation satellite system monitoring of the atmosphere, Elsevier, 2022, https://doi.org/10.1016/B978-0-12-819152-1.09995-5.
[3] M.R. Pearlman, J.J. Degnan, J.M. Bosworth, The international laser ranging service, Adv. Space Res. 30 (2) (2002) 135–143, https://doi.org/10.1016/S0273-1177(02)00277-6.
[4] H. Schuh, D. Behrend, VLBI: a fascinating technique for geodesy and astrometry, J. Geodyn. 61 (2012) 68–80, https://doi.org/10.1016/j.jog.2012.07.007.
[5] P. Willis, F.G. Lemoine, G. Moreaux, et al., The International DORIS Service (IDS), recent developments in preparation for ITRF2013, IAG SYMP. 143 (2015) 631–639, https://doi.org/10.1007/1345_2015_164.
[6] J.L. Davis, B.P. Wernicke, M.E. Tamisiea, On seasonal signals in geodetic time series, J. Geophys. Res. 117 (2012), https://doi.org/10.1029/2011jb008690.
[7] J. Bogusz, M. Figurski, Annual signals observed in regional GPS networks, Acta Geodyn. Geomater. 11 (2) (2014) 125–131, https://doi.org/10.13168/AGG.2014.0003.
[8] S. Khelifa, S. Kahlouche, M.F. Belbachir, Analysis of position time series of GPS-DORIS co-located stations, Int. J. Appl. Earth Obs. Geoinf. 20 (2013) 67–76, https://doi.org/10.1016/j.jag.2011.12.011.
[9] A. Klos, M.S. Bos, J. Bogusz, Detecting time-varying seasonal signal in GPS position time series with different noise levels, GPS Solut. 22 (21) (2018), https://doi.org/10.1007/s10291-017-0686-6.
[10] T.M. Van Dam, G. Blewitt, M.B. Heflin, Atmospheric pressure loading effects on the global positioning system coordinate determinations, J. Geophys. Res. 99 (B12) (1994) 23939–23950, https://doi.org/10.1029/94JB02122.
[11] J. Bogusz, A. Klos, On the significance of periodic signals in noise analysis of GPS station coordinates time series, GPS Solut. 20 (2016) 655–664, https://doi.org/10.1007/s10291-015-0478-9.
[12] S. Khelifa, Noise in DORIS station position time series provided by IGN-JPL, INASAN and CNES-CLS Analysis Centres for the ITRF2014 realization, Adv. Space. Res. 58 (12) (2016) 2572–2588, https://doi.org/10.1016/j.asr.2016.06.004.
[13] S.D.P. Williams, P. Willis, Error analysis of weekly station coordinates in the DORIS network, J. Geod. 80 (2006) 525–539, https://doi.org/10.1007/s00190-006-0056-6.
[14] K. Le Bail, Estimating the noise in space-geodetic positioning: the case of DORIS, J. Geod. 80 (2006) 541–565, https://doi.org/10.1007/s00190-006-0088-y.
[15] A. Klos, J. Bogusz, G. Moreaux, Stochastic models in the DORIS position time series: estimates for IDS contribution to ITRF2014, J. Geod. 92 (2018) 743–763, https://doi.org/10.1007/s00190-017-1092-0.
[16] S.D.P. Williams, Y. Bock, P. Fang, et al., Error analysis of continuous GPS position time series, J Geophys Res 109 (B3) (2004) B03412, https://doi.org/10.1029/2003JB002741.
[17] M. Feissel-Vernier, O. de Viron, K. Le Bail, Stability of VLBI, SLR, DORIS, and GPS positioning, Earth Planets Space 59 (2007) 475–497, https://doi.org/10.1186/BF03352712.
[18] A. Mao, C.G.A. Harrison, T.H. Dixon, Noise in GPS coordinate time series, J. Geophys. Res. 104 (B2) (1999) 2797–2816, https://doi.org/10.1029/1998JB900033.
[19] D.W. Allan, Time and frequency characterization, estimation and prediction of precision clocks and oscillators, IEEE Trans. UFFC 34 (6) (1987) 647–654, https://doi.org/10.1109/T-UFFC.1987.26997.
[20] M.S. Bos, L. Bastos, R.M.S. Fernandes, The influence of seasonal signals on the estimation of the tectonic motion in short continuous GPS time-series, J. Geodyn. 49 (2010) 205–209, https://doi.org/10.1016/j.jog.2009.10.005.
[21] T. Kall, T. Oja, K. Kolo, The noise properties and velocities from a time-series of Estonian permanent GNSS stations, Geosci. 9 (5) (2019) 233, https://doi.org/10.3390/geosciences9050233.
[22] J.D. Ray, M.S.M. Vijayan, A. Kumar, Noise characteristics of GPS time series and their influence on velocity uncertainties, J. Earth Syst. Sci 28 (2019) 146, https://doi.org/10.1007/s12040-019-1179-5.
[23] S.A. Ghasemi Khalkhali, A.A. Ardala, R. Karimi, A time series analysis of permanent GNSS stations in the northwest network of Iran, Ann. Geophys. 64 (2) (2021) GD218, https://doi.org/10.4401/ag-8450.
[24] R. Vautard, P. Yiou, M. Ghil, Singular-spectrum analysis: a toolkit for short, noisy, chaotic signals, Phys. D 58 (1992) 95–126, https://doi.org/10.1016/0167-2789(92)90103-T.
[25] S.A. Mallat, Theory for multiresolution signal decomposition: the wavelet representation, IEEE Trans. Pattern Anal. 11 (7) (1989) 674–693, https://doi.org/10.1109/34.192463.
[26] M. Ghil, M.R. Allen, M.D. Dettinger, et al., Advanced spectral methods for climatic time series, Rev. Geophys. 40 (1) (2002) 1–11, https://doi.org/10.1029/2000RG000092.
[27] S. Mallat, in: A wavelet tour of signal processing, third ed., Academic Press, USA, 2009.
[28] S. Khelifa, B. Gourine, A. Rami, H. Taibi, Assessment of nonlinear trends and seasonal variations in global sea level using singular spectrum analysis and wavelet multiresolution analysis, Arabian J. Geosci. 9 (2016) 560, https://doi.org/10.1007/s12517-016-2584-6.
[29] C. Noll, L. Soudarin, On-line resources supporting the data, products, and information infrastructure for the international DORIS service, J. Geod. 80 (8–11) (2006) 419–427, https://doi.org/10.1007/s00190-006-0051-y.
[30] G. Moreaux, F.G. Lemoine, H. Capdeville, et al., The International DORIS Service contribution to the 2014 realization of the International Terrestrial Reference Frame, Adv. Space. Res. 58 (12) (2016) 2479–2504, https://doi.org/10.1016/j.asr.2015.12.021.
[31] Z. Altamimi, P. Rebischung, L. Métivier, et al., ITRF2014: a new release of the international terrestrial reference frame modeling nonlinear station motions, J. Geophys. Res. Solid Earth 121 (B8) (2016) 6109–6131, https://doi.org/10.1002/2016JB013098.
[32] G. Moreaux, F.G. Lemoine, H. Capdeville, et al., The international DORIS service contribution to ITRF2020, Adv. Space Res. 72 (1) (2023) 65–91, https://doi.org/10.1016/j.asr.2022.07.012.
[33] G.F. Sella, T.H. Dixon, A. Mao, REVEL: a model for recent plate velocities from space geodesy, J. Geophys. Res. 107 (B4) (2002), https://doi.org/10.1029/2000JB000033. ETG 11-1–ETG 11-30.
[34] D.F. Argus, R.G. Gordon, M.B. Heflin, et al., The angular velocities of the plates and the velocity of the Earth's centre from space geodesy, Geophys J Int 180 (3) (2010) 913–960, https://doi.org/10.1111/j.1365-246X.2009.04463.x.
[35] Z. Altamimi, L. Métivier, P. Rebischung, et al., ITRF2020 plate motion model, Geophys. Res. Lett. 50 (2023), https://doi.org/10.1029/2023GL106373 e2023GL106373.
[36] C. DeMets, R.G. Gordon, D.F. Argus, et al., Effect of recent revisions to the geomagnetic reversal time scale on estimates of current plate motions, Geophys. Res. Lett. 21 (1994) 2191–2194, https://doi.org/10.1029/94GL02118.
[37] C. DeMets, R.G. Gordon, D.F. Argus, Geologically current plate motions, Geophys. J. Int. 181 (1) (2010) 1–80, https://doi.org/10.1111/j.1365-246X.2009.04491.x.

[38] C. Kreemer, G. Blewitt, E.C. Klein, A geodetic plate motion and Global Strain Rate Model, G-cubed 15 (10) (2014) 3849–3889, https://doi.org/10.1002/2014GC005407.
[39] H. Hassani, S. Heravic, A. Zhigljavskya, Forecasting European industrial production with singular spectrum analysis, Int. J. Forecast. 25 (2009) 103–118, https://doi.org/10.1016/j.ijforecast.2008.09.007.
[40] H. Hassani, R. Mahmoudvand, M. Zokaei, Separability and window length in singular spectrum analysis, C. R. Math. 349 (17–18) (2011) 987–990, https://doi.org/10.1016/j.crma.2011.07.012.
[41] Y. Meyer, in: Les Ondelettes : algorithmes et Applications, second ed., Armand Colin, Paris, 1994.
[42] M. Holschneider, Wavelets: an analysis tool, Oxford University Press, USA, 1999.
[43] I. Daubechies, in: Ten lectures on wavelets, SIAM) ed., Society for Industrial and Applied Mathematics, Philadelphia, USA, 1992.
[44] A. Antoniadis, Smoothing noisy data with coiflets, Stat. Sin. 4 (2) (1994) 651–678.
[45] H. Hassani, Singular spectrum analysis: methodology and comparison, J. Data Sci. 5 (2) (2007) 239–257, https://doi.org/10.6339/JDS.2007.05(2).396.
[46] G. Moreaux, F.G. Lemoine, D.F. Argus, et al., Horizontal and vertical velocities derived from the IDS contribution to ITRF2014, and comparisons with geophysical models, Geophys. J. Int. 207 (1) (2016) 209–227, https://doi.org/10.1093/gji/ggw265.
[47] P. Bird, An updated digital model of plate boundaries, G-cubed 4 (3) (2003) 1027, https://doi.org/10.1029/2001GC000252.
[48] P. Stepanek, J. Dousa, V. Filler, SPOT-5 DORIS oscillator instability due to South Atlantic anomaly: mapping the effect and application of data corrective model, Adv. Space. Res. 52 (7) (2013) 1355–1365, https://doi.org/10.1016/j.asr.2013.07.010.
[49] G. Blewitt, W.C. Hammond, C. Kreemer, Harnessing the GPS data explosion for interdisciplinary science, Eos 99 (2018), https://doi.org/10.1029/2018EO104623.
[50] A. Couhert, F. Mercier, J. Moyard, R. Biancale, Systematic error mitigation in DORIS-derived geocenter motion, J. Geophys. Res. Solid Earth 123 (11) (2018) 10142–10161, https://doi.org/10.1029/2018JB015453.
[51] M.L. Gobinddass, P. Willis, O. de Viron, et al., Sysematic biases in DORIS-derived geocenter time series related to solar radiation pressure mismodeling, J. Geod. 83 (9) (2009) 849–858, https://doi.org/10.1007/s00190-009-0303-8.
[52] H. Capdeville, P. Stepanek, L. Hecker, et al., Update of the corrective model for Jason-1 DORIS data in relation to the South Atlantic Anomaly and a corrective model for SPOT-5, Adv. Space. Res. 58 (12) (2016) 2628–2650, https://doi.org/10.1016/j.asr.2016.02.009.
[53] J. Saunier, The DORIS network: advances achieved in the last fifteen years, Adv Space Res 72 (1) (2023) 3–22, https://doi.org/10.1016/j.asr.2022.07.016.
[54] Y.V. Yasyukevich, B. Zhang, V.R. Devanaboyina, Advances in GNSS positioning and GNSS remote sensing, Sensors 24 (4) (2024) 1200, https://doi.org/10.3390/s24041200.
[55] L. Caron, E.R. Ivins, E. Larour, et al., GIA model statistics for GRACE hydrology, cryosphere, and ocean science, Geophys. Res. Lett. 45 (5) (2018) 2203–2212, https://doi.org/10.1002/2017GL076644.

Sofiane Khelifa is a Research Director at the Department of Space Geodesy at the Centre of Space Techniques (Algeria). His main area of interest is the analysis and diagnosis of position time series of space geodetic stations (VLBI, SLR, GPS and DORIS) in order to assess their systematic signals (trends and seasonal components) and their noise.